Enhanced Grain Size, Photoluminescence, and Photoconversion Efficiency with Cadmium Addition during the Two-Step Growth of CH$_3$NH$_3$PbI$_3$

Suneth C. Watthage, Zhaoning Song, Niraj Shrestha, Adam B. Phillips, Geethika K. Liyanage, Paul J. Roland, Randy J. Ellingson, and Michael J. Heben*

Wright Center for Photovoltaics Innovation and Commercialization, School of Solar and Advanced Renewable Energy, Department of Physics and Astronomy, University of Toledo, Toledo, Ohio 43606, United States

S *Supporting Information*

ABSTRACT: Control over grain size and crystallinity is important for preparation of methylammonium lead iodide (MAPbI$_3$) solar cells. We explore the effects of using small concentrations of Cd^{2+} and unusually high concentrations of methylammonium iodide during the growth of MAPbI$_3$ in the two-step solution process. In addition to improved crystallinity and an enhancement in the size of the grains, time-resolved photoluminescence measurements indicated a dramatic increase in the carrier lifetime. As a result, devices constructed with the Cd-modified perovskites showed nearly a factor of 2 improvement in the power conversion efficiency (PCE) relative to similar devices prepared without Cd addition. The grains also showed a higher degree of orientation in the ⟨110⟩ direction, indicating a change in the growth mechanism, and the films were compact and smooth. We propose a Cd-modified film growth mechanism that invokes a critical role for low-dimensional Cd perovskites to explain the experimental observations.

KEYWORDS: perovskite, grain growth, carrier lifetime, cadmium incorporation, low-dimensional perovskites, two-step deposition, nonradiative recombination
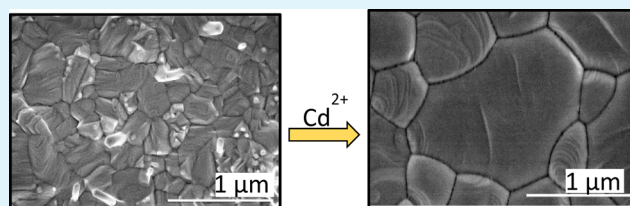
INTRODUCTION

Thin film solar cells based on organic–inorganic metal halide perovskites have become highly attractive over the past several years with solar to electric power conversion efficiencies (PCEs) reaching 22.1%.[1] Methylammonium lead iodide (CH$_3$NH$_3$PbI$_3$, MAPbI$_3$) and related perovskite materials possess high absorption coefficients, long minority carrier lifetimes and diffusion lengths, and desirable optical band gaps, and carrier collection can be highly efficient when these materials are paired with appropriate electron and hole transport layers (ETLs and HTLs, respectively).[2−7] Moreover, MAPbI$_3$ solar cells can be fabricated via solution-based routes, with the potential for low-cost scale-up to large area manufacturing. This combination of attributes may give perovskite solar cells (PSCs) an advantage over currently available commercial photovoltaic (PV) technologies. Importantly, recent life cycle assessment studies show that the toxicity impact of the lead used in the formation of the absorber layer is negligible[8] and that perovskite solar modules possess the shortest energy payback time.[9]

Several challenges must be overcome before the full potential of PSCs can be realized. Composition control is important to avoid the presence of undesirable phases,[10,11] and morphology control is desired to achieve smooth, continuous, and compact perovskite films to avoid shunts and reduce surface recombination rates.[12,13] Control over grain size and crystallinity is extremely important for reducing the density of charge traps, which can control the recombination rates of photoexcited carriers.[14,15]

The development of the two-step deposition method by Burschka et al. was a major advance in perovskite film formation.[3] In their pioneering work, a PbI$_2$ layer was spin-coated from a dimethylformamide (DMF) solution onto a mesoporous TiO$_2$ film and then converted to MAPbI$_3$ by exposure to methylammonium iodide (MAI). With this approach, the PCE of MAPbI$_3$ perovskite solar cells was immediately improved from 12% to 15%.[3] The approach relied upon the formation of a thin (150−300 nm) mesoporous TiO$_2$ layer with high transparency and electron mobility. Such films are a byproduct of tremendous research in the dye-sensitized solar cell community and have been achieved in only a few laboratories.[3,4,16,17] PCEs have been pushed to 17% with this approach in the basic MAPbI$_3$ device.[4] An optimized mesoporous TiO$_2$ scaffold allows the PbI$_2$ solution to partially penetrate so that a high surface area PbI$_2$ film can be formed. Such a film can be converted into the perovskite phase upon exposure to MAI, although the resultant grains are still relatively small (c.a. 100−300 nm). In an effort to produce
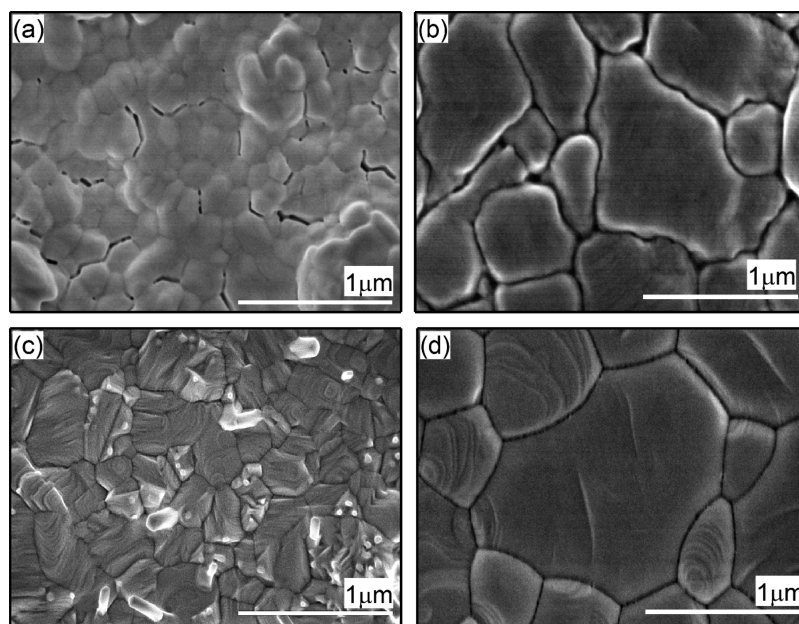
Figure 1. SEM images of the surface of as-spun MAPbI$_3$ thin films prepared (a) without and (b) with 10 mM CdCl$_2$ addition to the MAI solution. Panels (c) and (d) show the data corresponding to (a) and (b), respectively, after heating to 150 °C.

high efficiency devices in the so-called planar structure, that is, without fabrication of the mesoporous TiO$_2$ layer, investigators have engineered porosity into the PbI$_2$ layer by adding *n*-butanol,[18] MAI,[19] or 4-*tert*-butylpyridine[20] to the PbI$_2$/DMF precursor solution, or by employing DMSO as a solvent.[21] The resulting high surface area porous PbI$_2$ layers can also be readily converted to MAPbI$_3$, but, once again, the resultant grains are not as large as desired. Even with porous layers there is a need to balance the degree of PbI$_2$ conversion while seeking to avoid the formation of MAI-rich precipitates that lead to poor device behavior. Consequently, researchers typically use MAI concentrations of 50–70 mM to optimize the PCE.[18−20] Without porosity in the PbI$_2$ layer, MAI diffusion is hindered and the conversion to MAPbI$_3$ is incomplete.[20,22] Interestingly, Zhang et al. produced devices with PCEs of 1.5% or 10.7% depending on whether the PbI$_2$ seed layer was compact or porous.[20]

In an effort to decouple the perovskite conversion process from the need to prepare PbI$_2$ in a porous configuration, we explored the effects of including small concentrations of Cd^{2+} into unusually high concentration MAI (250 mM) solutions. We found that the large grains could be retained by including small concentrations of CdCl$_2$ into the MAI solutions, and that a high degree of PbI$_2$ conversion could be achieved without the formation of deleterious MAI-rich precipitates. In addition, the solution-phase Cd incorporation route also led to a dramatic enhancement in the carrier lifetime as determined by time-resolved photoluminescence (TRPL) measurements. As a result, the PCE of finished devices was enhanced by nearly a factor of 2 relative to devices constructed without Cd addition. The grains also showed a very high degree of orientation in the ⟨110⟩ direction, and the films were more compact and smooth. To explain the experimental results, we propose a film growth mechanism that invokes a critical role for low-dimensional Cd perovksites.

■ RESULTS AND DISCUSSION

Samples were prepared on compact TiO$_2$ (c-TiO$_2$) coated F-doped SnO$_2$ (FTO)/glass substrates as described in detail in the Experimental Section. Briefly, the PbI$_2$ seed layer (∼350 nm) was prepared on a c-TiO$_2$ layer (∼50 nm) by spin-coating 100 μL of a 70 °C solution of 1 M PbI$_2$ in DMF. Following a heat treatment at 100 °C for 15 min to evaporate the solvent, 500 μL of a 70 °C, 250 mM MAI in isopropanol (IPA) solution, with and without 10 mM CdCl$_2$, was then spin-coated onto the PbI$_2$ seed layer. Note that other concentrations were also examined, but 10 mM CdCl$_2$ was found to produce the best results (Figure S1). Samples were then heated to 150 °C for 5 min to complete the MAPbI$_3$ perovskite formation reaction. All material depositions and heat treatments, except for the c-TiO$_2$ growth, were performed in a water and oxygen-free (∼0.1 ppm) N$_2$-filled glovebox. The resultant films were characterized by scanning electron microscopy (SEM), energy dispersive X-ray spectroscopy (EDS), X-ray diffraction (XRD), UV−vis spectroscopy, and steady-state and time-resolved photoluminescence (PL and TRPL, respectively).

Figure 1 compares the SEM images of the perovskite films formed with and without 10 mM CdCl$_2$ in the MAI solution that was used to convert the PbI$_2$ seed layer. The effect of the CdCl$_2$ addition is evident in that well-defined, large grains are present in the Cd incorporated samples (Cd_MAPbI$_3$) immediately after spinning, while samples prepared without CdCl$_2$ show poorly defined and poorly crystalline films with obvious gaps between grains. The inclusion of 10 mm CdCl$_2$ increased the grain sizes 5-fold, from ∼200 nm to ∼1 μm. After the 150 °C step that is conventionally used to complete the perovskite formation in the two-step process, SEM showed that the crystallinity in the samples formed without CdCl$_2$ (Figure 1c) had improved dramatically even though the grain size was not substantially increased. Similarly, the grain size of the as-deposited film produced with CdCl$_2$ was also not substantially increased with the 150 °C reaction step (Figure 1d). However, there is evidence for smaller grains having merged into larger ones, and the spaces between grains have been more

completely filled and the film is more dense and compact. An additional significant change is the improved electrical conductivity at the grain boundary edges. Before heating, Cd_MAPbI₃ films showed high contrast at the grain edges, consistent with charging during SEM imaging.

XRD (Figure 2a) confirmed that the degree of crystallinity was dramatically improved when CdCl₂ was added to the MAI
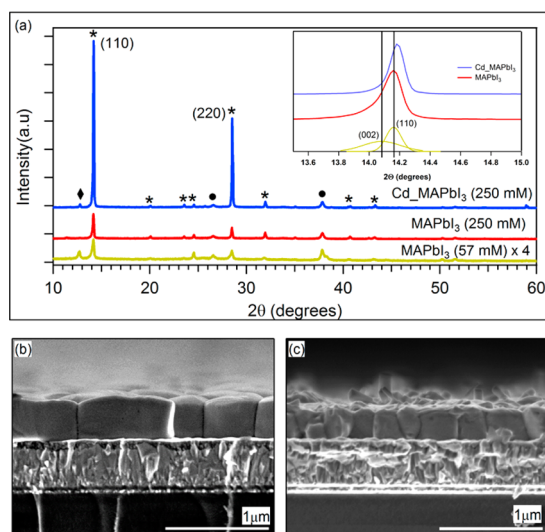
Figure 2. (a) X-ray diffraction spectra of MAPbI₃ perovskite films prepared with the standard and Cd-modified two-step deposition methods after the postdeposition heating. The spectrum for the material prepared with 57 mM MAI was multiplied by a factor of 4 to allow the peaks to be clearly seen on the same scale. The characteristic XRD peaks belong to MAPbI₃ perovskite (★), PbI₂ (◆), and FTO/c-TiO₂ substrate (●). (b and c) Cross-sectional SEM images of MAPbI₃ perovskite thin films prepared by two-step spin-coating method (b) with and (c) without addition of 10 mM CdCl₂ (after the postdeposition heating).

solution. Both Cd_MAPbI₃ and MAPbI₃ films showed characteristic X-ray peaks for the tetragonal perovskite phase (space group $I4/mcm$),[11,23] but the intensity of the (110) peak at $2\theta = 14.1°$ was larger by a factor of ∼6.5 for the Cd_MAPbI₃ film, and its full-width-half-maximum value was reduced by a factor of 1.6. Similar changes were observed for the (220) diffraction peak. In addition to a much higher degree of crystallinity, the data indicate that the crystallites comprising the Cd_MAPbI₃ film are nearly completely oriented along the ⟨110⟩ direction. In contrast, the crystallites produced without Cd exhibited more random orientations (see Table S1). For comparison, Figure 2a also shows the XRD pattern that resulted when the PbI₂ films were processed with 57 mM MAI. In this case, the poor crystallinity and the remaining PbI₂ are clearly evident. The highest intensity peak at $2\theta = 14.1°$ can be deconvoluted into two components from (002) and (110) planes (see Figures 2a and S4), which is a characteristic feature of the tetragonal structure.[11] With the addition of Cd²⁺, the (110) peak shifted to higher values of 2θ. This is likely due to a change in the lattice parameter associated with substitution of the smaller Cd²⁺ species onto Pb²⁺ sites.

Cross-sectional SEM images revealed that single, flat-topped grains extended through the entire film thickness when CdCl₂ was employed (Figure 2b), while the grains were jumbled and less well organized for the conventional MAPbI₃ synthesis (Figure 2c). The cross-sectional images also revealed that the

film thickness had also increased by ∼100 nm when Cd was used. Evidently, Cd incorporation improves grain growth in both lateral and vertical directions, resulting in the formation of a larger volume of perovskite material.

To determine that Cd, rather than Cl,[24,25] was responsible for the observed changes in film growth, we prepared additional films using Cd(CH₃CO₂)₂ (cadmium acetate) and methylammonium chloride (CH₃NH₃Cl) as additives to the MAI solution. Concentrations were chosen to produce the same Cd and Cl concentrations as was experienced with CdCl₂. The perovskite films prepared with Cd(CH₃CO₂)₂ showed an enhancement in the grain size and crystallinity similar to that found with CdCl₂, while no change in the films characteristics relative to the control preparation was observed when CH₃NH₃Cl was employed (see Figure S2c,d). Consequently, we can be confident that Cd species, rather than Cl, are responsible for these observations.

PL and TRPL measurements were performed to determine the effect of Cd incorporation on the optoelectronic properties of the perovksite films. For these measurements, the films were deposited on soda-lime glass without electron and hole transport layers in an effort to minimize carrier collection at the surfaces and allow the intrinsic characteristics of the perovskite film to govern the recombination kinetics (see the Experimental Section). The PL emission (Figure 3a) from the
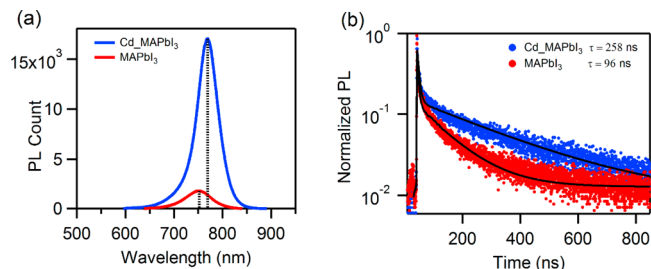
Figure 3. (a) Steady-state PL spectra from sample excited with 140 mW/cm² of 532 nm laser light and (b) intensity-normalized time-resolved PL decay measured from the longest mean lifetime MAPbI₃ and Cd_MAPbI₃ samples excited with ∼10¹⁰ photons/pulse/cm² at the peak emission wavelength, as determined from the steady-state PL measurement shown in part (a) (see the Experimental Section for more details).

MAPbI₃ films made without Cd was relatively weak and centered at 753 nm, while the PL emission from Cd_MAPbI₃ samples was red-shifted to 768 nm, narrower, and more intense by a factor of ∼9. The increase in PL intensity and the reduction in the line width indicate a significant reduction in trap-mediated, nonradiative recombination.

Consistent with the steady-state PL data, TRPL measurements (Figure 3b) showed that the PL decay was significantly slowed in Cd_MAPbI₃ samples. The TRPL decays for both Cd_MAPbI₃ and MAPbI₃ samples were well-fit with a biexponential function having two decay constants (Table 1). The initial PL decay for both types of samples is associated with an initial relatively fast process with a time constant, τ_1, of ∼5–6 ns. This fast decay may be due to Auger recombination associated with the initially high population of carriers in the excitation volume. After the initial fast decay, there is a slow decay component with a time constant, τ_2, that is very different in the two kinds of films. While the MAPbI₃ films formed by the standard two-step deposition process showed a slow decay time constant of 103 ns, τ_2 for the sample prepared with Cd

Table 1. Biexponential Fitting Time Constants and Mean Lifetime of the Carriers[a]

sample	τ_1 (ns)	yield 1 (%)	τ_2 (ns)	yield 2 (%)	mean lifetime (ns)
standard perovskite	5.2	18	103	82	86
Cd-modified perovskite	6.3	12	266	88	237

[a]Average over three different sample spots.

had a value of 266 ns. Furthermore, the yield of the long-lifetime component was also improved for the Cd_MAPbI$_3$ samples, from 82% to 88%. Overall, Cd inclusion increased the mean lifetime (Table 1) from 86 to 237 ns, an increase of nearly a factor of 3. The increase in PL intensity and lifetime indicates that the nonradiative recombination rates have been slowed in the Cd_MAPbI$_3$ samples. Unfortunately, there are no data in the literature that allow us to compare our findings to theoretical expectations for defect levels that might be introduced during Cd substitution for Pb, although Shi et al.[26] did comment that substitution could occur. Our observation of longer PL lifetimes with Cd substitution suggests that no new defects are introduced. Furthermore, the red-shift in the PL emission that is observed can be favorably compared to the band gap reduction that has been calculated by Navas et al.[27] for Cd substitution in Pb-based perovskites.

To develop an understanding of the mechanism that leads to the enhancement in grain size and crystallinity, we first consider the basic nucleation and growth mechanisms of MAPbI$_3$ perovskite in the two-step process without Cd. Once MAI is introduced to the PbI$_2$ seed layer, MAI interacts with the PbI$_2$ framework to form the perovskite phase. The density of MAPbI$_3$ nuclei is determined by the concentration of MAI in the IPA solution.[4] At high MAI concentrations, the PbI$_2$ can be partially dissolved, and the nucleation of the MAPbI$_3$ can be viewed as occurring in a nearly homogeneous manner.[22] In this case, a relatively large number of nuclei are created, there is little preferred orientation, and the grain growth is diffusion limited. Under these conditions, the perovskite film is comprised of relatively small, randomly oriented grains. Additional consideration of the phase diagram[11] indicates that low-dimensional perovskites (LDPs) are present when the MAI concentration is high. Consequently, the as-deposited film is highly defective and poorly ordered (Figures 1a and S2f). The LDPs and small crystallites can be converted into material with improved crystallinity and higher electronic quality by simple postdeposition heat treatment (Figures 1c and 2c).

The dramatic improvement in grain size observed when Cd is included is clearly connected to a change in the growth process. Heterogeneous nucleation is suggested by the fact that the addition of Cd to the MAI solution leads to MAPbI$_3$ films that are highly oriented. However, note that the PbI$_2$ film is oriented in the ⟨001⟩ direction, which would be consistent with templating of (202) perovskite planes (see Figures S3 and S4), but the Cd_MAPbI$_3$ films are oriented in the ⟨110⟩ direction. Note also that the grain sizes and shapes are very different in the PbI$_2$ and Cd_MAPbI$_3$ films. While the Cd_MAPbI$_3$ films are compact with 1–2 μm grains, the PbI$_2$ seed layer is terraced and slightly porous (~6%)[28] with grain sizes on the order of a few hundred nanometers (see Figure S2a,b).

To develop more insight, optical absorption spectroscopy was performed on the Cd-containing MAI solutions.

Absorption in the range of 300−325 nm was ascribed to the formation of molecular complexes (see Figure S5). The solutions were optically clear for at least a week, indicating that the Cd-based MAI complexes do not interact or coalesce. In contrast, addition of 10 mM Pb ions to MAI solutions led to turbid solutions and precipitation, indicating the growth of larger particles. Evidently, the surfaces of the Cd complexes are terminated in such a way that they are less reactive than their Pb counterparts such that they do not readily agglomerate. X-ray studies of films formed by deposition of the Cd-MAI complexes onto glass substrates (see Figure S7) revealed diffraction peaks at 2θ of 9.1°, 16.7°, and 25.2°. The XRD pattern indicates that the solution phase complexes are most likely Cd-based LDPs such as $(CH_3NH_3)_2CdI_4$.[29,30] Note that similar X-ray signals were also observed in the as-deposited Cd_MAPbI$_3$ films, but they disappeared after the films were subjected to the mild postdeposition heating (see Figure S7). Thermal gravimetric analysis (TGA) showed that the decomposition of the $(CH_3NH_3)_2CdI_4$ material initiated at ~200 °C, in strong similarity to TGA data for MAPbI$_3$[11] (see Figure S8).

With all of the data in hand, we can speculate on a possible mechanism by which the small grain ⟨001⟩ oriented PbI$_2$ seed layer can be transformed into the large, compact grains of MAPbI$_3$ with nearly complete ⟨110⟩ orientation. First, because the growth of the large oriented grains occurs immediately upon introduction of the Cd-containing MAI solution, without the need for any annealing process, it is very likely that the PbI$_2$ film is not dissolved, reacted, and reprecipitated as MAPbI$_3$. This so-called dissolution/precipitation reaction has been evoked to describe the growth of the smaller, randomly oriented crystallites that typically result from the two-step process[22] (Figures 1c and 2c). As an alternative, we can consider a process in which the PbI$_6$ octahedra that comprise the PbI$_2$ are not moved significantly from their initial positions but, instead, are rotated and transition from edge sharing to corner sharing coordination with incorporation of MAI. In this view, the large grain sizes are a consequence of the conversion of the ⟨001⟩ PbI$_2$ seed layer proceeding in an organized fashion as might be expected for a topotactic process. Apparently, the Cd-LDPs serve as a type of flux or catalyst for enabling the transformation. The concept is similar to the solution−liquid−solid growth mechanism that has been developed for understanding the growth of III−V crystals.[31] In the present case, the fluxing species is the Cd-LDPs, which are formed in the MAI solution. When the MAI solution is introduced to the PbI$_2$ seed layer, the Cd-LDPs will have a high affinity for the PbI$_2$ terrace edges. At the interface, mixed-metal LDPs may form with some degree of interdiffusion. Because the $(CH_3NH_3)_2CdI_4$ structure consists of cadmium iodide octahedra nanostructures (sheets) encased in an organic MA$^+$ matrix in an open configuration,[30] Cd-LDPs interfaced to PbI$_2$ grains should provide low energy pathways for incorporation and transport of MA$^+$ and I$^-$ species. In this way, the phase transformation of the parent PbI$_2$ film to MAPbI$_3$ would be facilitated. The difference in grain size of the initial PbI$_2$ and final MAPbI$_3$ films can be rationalized by two-dimensional annealing that could be additionally facilitated by the presence of the Cd-LDP flux. This recrystallization process fills the pin-holes and voids between grains, resulting in the observed large grains with a reduced grain boundary area. Returning to the SEM image of Figure 1b, the high contrast edges of the grains in the as-deposited Cd_MAPbI$_3$ film can now be understood as

being due to the presence of electrically insulating Cd-LDPs that are left decorating the edges of the grains. Interestingly, EDS scans of both surface and cross-sectional views did not detect any Cd, indicating that the Cd concentration is below 1%. The subsequent heat treatment decomposes the LDP structure and integrates the Cd more fully into the $MAPbI_3$ structure (Figure 1d).

To determine the impact of the increased grain size and carrier lifetime on the photovoltaic device performance, solar cells were fabricated on the basis of Cd_MAPbI_3 and $MAPbI_3$ thin films in the FTO/c-TiO_2/m-TiO_2/$MAPbI_3$/spiro-MeO-TAD/Au configuration. The ~150 nm thick mesoporous TiO_2 layer (m-TiO_2) was formed by spin-coating TiO_2 paste (Dyesol 18NR-T) diluted in ethanol onto the c-TiO_2 layer and annealing at 550 °C for 30 min (see the Experimental Section for complete device fabrication). Current−voltage (J−V) was collected under simulated AM 1.5G solar spectrum at light intensity of 100 mW/cm². We note that this nonoptimized cell configuration with a relatively thin mesoporous layer was adopted to allow relatively high throughput experimentation and investigation of the impacts of the Cd-induced grain growth. Figure 4 shows that the PCEs for the 30 full devices fell
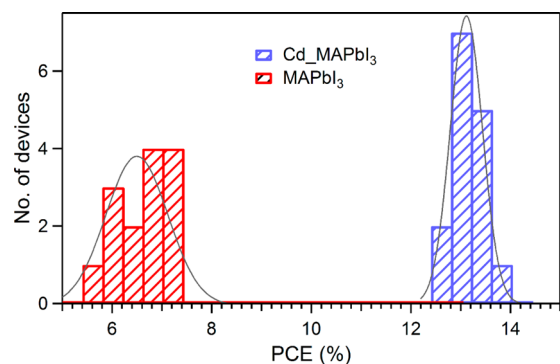
Figure 4. Histogram of efficiencies for devices prepared from $MAPbI_3$ and Cd_MAPbI_3 thin films.

into two narrow and distinct ranges. Note that the low PCE for the devices formed without Cd (~7%) using 250 mM MAI should be compared to a value of 10.8%, which is typical for cells made on TiO_2 layers produced in our laboratories using an MAI concentration that optimizes efficiency without Cd (57 mM, see Figure 2a). This latter value can then be compared to a state-of-the-art device formed with similar processing but with a more fully optimized TiO_2 electron transfer bilayer (15−17%).[3,4] Devices made from Cd_MAPbI_3 with 10 mM $CdCl_2$ and 250 mM MAI yielded efficiencies that were approximately twice the average efficiency of the 250 mM MAI $MAPbI_3$ devices using a similarly unoptimized TiO_2 bilayer.

Table 2 shows that the improved PCE for the devices made with Cd_MAPbI_3 comes from increases in the open circuit

voltage (V_{OC}), short circuit current density (J_{SC}), and fill factor (FF). Note that a V_{oc} value of 1.06 V for the champion Cd_MAPbI_3 device is close to the current record of 1.15 V.[32] J−V hysteresis appeared in devices made with both the standard and the Cd-modified perovskite films (Figure S9), and the hysteresis factor[33] was slightly improved (from 42% to 39%) with the addition of Cd. With an average value of 17.8 mA/cm², which is substantially lower than the current record value of 23.5 mA/cm²,[32] it is clear that the J_{sc} is the primary factor that limits the performance of the devices.

To explore the origin of the low J_{sc} values, the external quantum efficiency (EQE) was measured. Consistent with the J−V measurements, the champion Cd_MAPbI_3 device showed an EQE response that was higher than the response of the champion $MAPbI_3$ device across the entire wavelength range (Figure 5). Of particular note is the long wavelength response, which is reduced for both devices. Poor long wavelength response is generally associated with poor collection of charge carriers that are generated deep within the device. The poor performance in the long wavelength region is, once again, consistent with the limitations of our TiO_2 bilayers. To estimate the internal quantum efficiency (IQE), the EQE data were corrected by the transmission spectrum data for the glass/FTO/c-TiO_2/m-TiO_2 portion of the device that reduces the amount of light admitted into the perovskite absorber (Figure 5).

The IQE data show that the current collection for the Cd_MAPbI_3 sample is fairly high across the full spectrum (average of 83% from 460 to 750 nm), while the IQE for the $MAPbI_3$ control device is still poor at wavelengths longer than ~450 nm. The poor long wavelength response from the control $MAPbI_3$ film indicates that the dominant recombination mechanism is associated with traps that reduce the probability of harvesting photoexcited electrons close to the HTL at the back of the device. Evidently, the inclusion of Cd during synthesis improves the collection of photoexcited electrons by reducing the effective density of charge traps. Because the transparent conductor/ETL portion of our devices has not been optimized for transmission, it is interesting to estimate the theoretical maximum for J_{sc} of the device by integrating the IQE data. In this case, we would expect a J_{sc} of 21.4 mA/cm², which would give rise to a 16.4% device with all other parameters held constant.

■ CONCLUSION

We have shown that Cd salts introduced into the MAI precursor solution can allow the use of higher MAI concentrations and significantly improve the quality of $MAPbI_3$ perovskite films prepared by the two-step method. The grain size and crystallinity were strongly enhanced, and the ⟨110⟩ oriented Cd-$MAPbI_3$ films exhibited increased carrier lifetimes and solar cell device efficiency with improved

Table 2. Solar Cell Performance Metric for Devices Made with Cd_MAPbI_3 and $MAPbI_3$ Films

sample	V_{oc} (V)	J_{sc} (mA/cm²)	FF (%)	PCE (%)
control				
average	0.91 ± 0.03	12.3 ± 1.4	58.65 ± 8.66	6.5 ± 0.7
champion	0.92	12.5	62.06	7.1
with $CdCl_2$				
average	1.04 ± 0.01	17.8 ± 0.3	70.42 ± 0.99	13.1 ± 0.3
champion	1.06	17.9	72.59	13.8
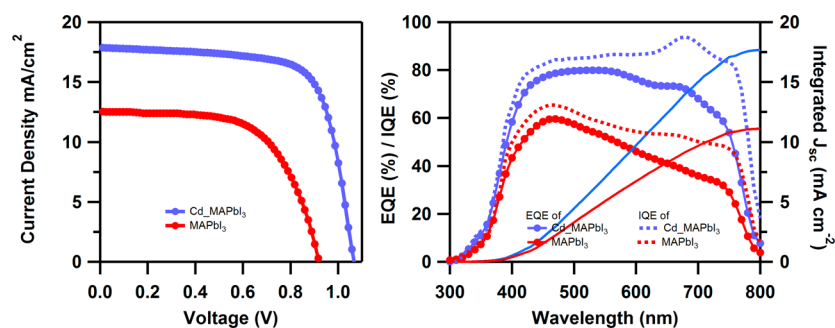
Figure 5. $J-V$ measurements, EQE, IQE spectra, and integrated current densities of $CH_3NH_3PbI_3$ perovskite solar cells with (blue) and without (red) $CdCl_2$ additives. The integrated photocurrent density values were 11.22 and 17.7 mA/cm^2 for devices prepared with standard and Cd-assisted MAPbI$_3$, respectively. These values were in good agreement with the experimentally measured J_{sc} values (Table 1).

reproducibility. Although not completely understood, the growth mechanism clearly changes, and the resultant films demonstrate improved carrier lifetimes. Using an unoptimized TiO$_2$ bilayer, we showed that the PCE of perovskite solar cells can be improved with Cd^{2+} incorporation during the film preparation. The Cd-assisted deposition method may provide a way to improve the quality of films grown by high rate deposition processes.

■ EXPERIMENTAL SECTION

Unless specified, all chemicals were obtained from Sigma-Aldrich and used without further purification.

Synthesis of Methylammonium Iodide. Methylammonium iodide was synthesized by reacting hydroiodic acid (HI, 57 wt % in water) with methylamine solution (CH$_3$NH$_2$, 33 wt % in ethanol) in an ice bath with continuous stirring for 2 h in a nitrogen atmosphere. A white product was obtained after evaporating the liquid phase at 80 °C. The product was then dissolved in ethanol and recrystallized using diethyl ether. Finally, the MAI powder was obtained after drying for more than 12 h in a vacuum.[34]

Perovskite Film Preparation. The 1 in. × 1 in. FTO coated glass substrates (TEC 15, Pilkington NA) were cleaned in an ultrasonic bath with Micro-90 detergent for 1 h and then rinsed for 1 h in deionized water. The samples were thoroughly dried using nitrogen gas and transferred to a nitrogen filled glovebox with (∼0.1 ppm of H$_2$O and O$_2$). An ∼50 nm thick compact TiO$_2$ film was prepared by spinning a 0.3 M titanium diisopropoxide bis(acetylacetonate) in ethanol onto the FTO substrates. The deposited layer was dried at 125 °C for 5 min and then annealed at 500 °C for 30 min in air.[35] The MAPbI$_3$ perovskite layer was formed by reacting a PbI$_2$ seed layer with a 250 mM solution of MAI in IPA. A mixture of MAI (250 mM) and CdCl$_2$ (10 mM) in IPA was used in the Cd-assisted deposition. The PbI$_2$ layer was deposited by spin-coating a hot (∼70 °C) solution of 1 M PbI$_2$ in anhydrous DMF at 5000 rpm for 30 s, followed by drying at 100 °C for 15 min. After being cooled to room temperature, the MAI-IPA solution (with and without CdCl$_2$) was preheated to 70 °C and spin-coated onto the PbI$_2$ layer. The reaction was completed by heating to 150 °C for 5 min on a hot plate.

Thin Film Characterization. SEM (Hitachi S-4800) images and XRD (Rigaku Ultima III) spectra were gathered from films prepared on FTO/glass substrates that were coated with a compact TiO$_2$ layer. Films were directly deposited onto soda-lime glass substrates to obtain UV−vis absorption (PerkinElmer Lambda 1050), PL, TRPL data of MAPbI$_3$ films, and XRD of (CH$_3$NH$_3$)$_2$CdI$_4$ LDPs.

PL measurements were obtained at several locations on the MAPbI$_3$ samples with 532 nm CW excitation from the film side (laser spot size of ∼140 μm, integration time of 0.5 s, laser intensity of 140 mW/cm^2) at room temperature. The PL signal was detected with a Symphony II CCD detector (Horiba) after a 300 g/mm grating monochromator. TRPL measurement at different locations of the samples was performed with a time correlated single photon counting module (Becker & Hickel Simple Tau SPCM 130-E/M module). A 532 nm

pulsed laser (beam diameter of ∼100 μm) was used as a source of excitation. Samples were excited with ∼10^{10} photons/pulse/cm^2 at the peak emission wavelength, as determined from the PL measurement. The PL signal was detected by PMT hybrid detector after a Horiba IHR 320 monochromator (900 g/mm, 850 nm blaze) grating. Decay curves were fitted to a biexponential decay function.

Device Preparation. After deposition of the compact TiO$_2$, an ∼150 nm thick mesoporous TiO$_2$ layer was deposited by spin-coating a diluted TiO$_2$ paste (Dyesol 18NR-T) in ethanol (1:7 w/w) at 5000 rpm for 30 s. The deposit was dried at 125 °C for 5 min prior to annealing in air at 550 °C for 30 min. MAPbI$_3$ absorber then was formed using the two-step solution method as described above. The hole transport layer was made by dissolving 73.3 mg of 2,2′,7,7′-tetrakis(N,N-di-p-methoxy-phenylamine)-9,9′-spirobifluorene (Spiro-MeOTAD) in 1 mL of chlorobenzene with two additives: a 28.8 μL aliquot of tert-butylpyridine and a 17.6 μL aliquot of a lithium bis(trifluoromethanesulfonyl)imide (Li-TFSI) solution in acetonitrile. The latter was obtained from a stock solution (520 mg Li-TFSI/mL). The film was formed by spinning 80 μL of the mixture at 3000 rpm for 30 s on the perovskite layer. Finally, devices were completed by depositing 40 nm of gold as a back electrode with a 0.08 cm^2 active area using thermal evaporation.

Device Characterization. $J-V$ characteristics were measured under simulated AM1.5G illumination using a Keithley 2440 digital source meter and a solar simulator (Newport model 91195A-1000). The light intensity of the simulator was calibrated using a standard Si solar cell. The EQE measurements were acquired from wavelength range of 300−800 nm using a PV Measurements Inc., model IVQE8-C QE system without bias voltage.

■ ASSOCIATED CONTENT

Ⓢ Supporting Information

The Supporting Information is available free of charge on the ACS Publications website at DOI: 10.1021/acsami.6b12627.

> Device performance with different CdCl$_2$ concentrations, SEM images (PbI$_2$ seed layer, MAPbI$_3$ prepared with cadmium acetate and methylammonium chloride, and cross-sectional views of as-deposited Cd_ MAPbI$_3$ and MAPbI$_3$ films), XRD spectra (as-deposited Cd_ MAPbI$_3$ and MAPbI$_3$ films, and (CH$_3$NH$_3$)$_2$CdI$_4$ LDP), UV−vis absorbance spectra (standard and Cd-modified MAPbI$_3$ films), orientation index analysis, TGA of (CH$_3$NH$_3$)$_2$CdI$_4$, and $J-V$ curves of champion devices in forward and reverse scan directions (PDF)

■ AUTHOR INFORMATION

Corresponding Author

*E-mail: michael.heben@utoledo.edu.

ORCID

Suneth C. Watthage: 0000-0001-8728-9561
Zhaoning Song: 0000-0002-6677-0994
Michael J. Heben: 0000-0002-3788-3471

Notes

The authors declare no competing financial interest.

■ REFERENCES

(1) Nrel Solar Efficiency Chart. http://www.nrel.gov/ncpv/images/efficiency_chart.jpg (accessed September 2016).

(2) Green, M. A.; Ho-Baillie, A.; Snaith, H. J. The Emergence of Perovskite Solar Cells. *Nat. Photonics* **2014**, *8*, 506−514.

(3) Burschka, J.; Pellet, N.; Moon, S.-J.; Humphry-Baker, R.; Gao, P.; Nazeeruddin, M. K.; Gratzel, M. Sequential Deposition as a Route to High-Performance Perovskite-Sensitized Solar Cells. *Nature* **2013**, *499*, 316−319.

(4) Im, J.-H.; Jang, I.-H; Pellet, N.; Gratzel, M.; Park, N.-G. Growth of $CH_3NH_3PbI_3$ Cuboids with Controlled Size for High-Efficiency Perovskite Solar Cells. *Nat. Nanotechnol.* **2014**, *9*, 927−932.

(5) Jeon, N. J.; Noh, J. H.; Kim, Y. C.; Yang, W. S.; Ryu, S.; Seok, S. I. Solvent Engineering for High-Performance Inorganic−Organic Hybrid Perovskite Solar Cells. *Nat. Mater.* **2014**, *13*, 897−903.

(6) Liu, M.; Johnston, M. B.; Snaith, H. J. Efficient Planar Heterojunction Perovskite Solar Cells by Vapour Deposition. *Nature* **2013**, *501*, 395−398.

(7) Song, Z.; Watthage, S. C.; Phillips, A. B.; Heben, M. J. Pathways toward High-Performance Perovskite Solar Cells: Review of Recent Advances in Organo-Metal Halide Perovskites for Photovoltaic Applications. *J. Photonics Energy* **2016**, *6*, 022001.

(8) Celik, I.; Song, Z.; Cimaroli, A. J.; Yan, Y.; Heben, M. J.; Apul, D. Life Cycle Assessment (LCA) of Perovskite PV Cells Projected from Lab to Fab. *Sol. Energy Mater. Sol. Cells* **2016**, *156*, 157−169.

(9) Gong, J.; Darling, S. B.; You, F. Perovskite Photovoltaics: Life-Cycle Assessment of Energy and Environmental Impacts. *Energy Environ. Sci.* **2015**, *8*, 1953−1968.

(10) Tsai, H.; Nie, W.; Cheruku, P.; Mack, N. H.; Xu, P.; Gupta, G.; Mohite, A. D.; Wang, H.-L. Optimizing Composition and Morphology for Large-Grain Perovskite Solar Cells Via Chemical Control. *Chem. Mater.* **2015**, *27*, 5570−5576.

(11) Song, Z.; Watthage, S. C.; Phillips, A. B.; Tompkins, B. L.; Ellingson, R. J.; Heben, M. J. Impact of Processing Temperature and Composition on the Formation of Methylammonium Lead Iodide Perovskites. *Chem. Mater.* **2015**, *27*, 4612−4619.

(12) Marinova, N.; Tress, W.; Humphry-Baker, R.; Dar, M. I.; Bojinov, V.; Zakeeruddin, S. M.; Nazeeruddin, M. K.; Gratzel, M. Light Harvesting and Charge Recombination in $CH_3NH_3PbI_3$ Perovskite Solar Cells Studied by Hole Transport Layer Thickness Variation. *ACS Nano* **2015**, *9*, 4200−4209.

(13) Fu, K.; Nelson, C. T.; Scott, M. C.; Minor, A.; Mathews, N.; Wong, L. H. Influence of Void-Free Perovskite Capping Layer on the Charge Recombination Process in High Performance $CH_3NH_3PbI_3$ Perovskite Solar Cells. *Nanoscale* **2016**, *8*, 4181−4193.

(14) Nie, W.; Tsai, H.; Asadpour, R.; Blancon, J.-C.; Neukirch, A. J.; Gupta, G.; Crochet, J. J.; Chhowalla, M.; Tretiak, S.; Alam, M. A.; Wang, H.-L.; Mohite, A. D. High-Efficiency Solution-Processed Perovskite Solar Cells with Millimeter-Scale Grains. *Science* **2015**, *347*, 522−525.

(15) Bi, C.; Wang, Q.; Shao, Y.; Yuan, Y.; Xiao, Z.; Huang, J. Non-Wetting Surface-Driven High-Aspect-Ratio Crystalline Grain Growth for Efficient Hybrid Perovskite Solar Cells. *Nat. Commun.* **2015**, *6*, 7747.

(16) Wang, J. T.-W.; Ball, J. M.; Barea, E. M.; Abate, A.; Alexander-Webber, J. A.; Huang, J.; Saliba, M.; Mora-Sero, I.; Bisquert, J.; Snaith, H. J.; Nicholas, R. J. Low-Temperature Processed Electron Collection Layers of Graphene/TiO_2 Nanocomposites in Thin Film Perovskite Solar Cells. *Nano Lett.* **2014**, *14*, 724−730.

(17) Yang, W. S.; Noh, J. H.; Jeon, N. J.; Kim, Y. C.; Ryu, S.; Seo, J.; Seok, S. I. High-Performance Photovoltaic Perovskite Layers Fabricated through Intramolecular Exchange. *Science* **2015**, *348*, 1234−1237.

(18) Wu, W.; Li, H.; Liu, S.; Zheng, B.; Xue, Y.; Liu, X.; Gao, C. Tuning PbI_2 Layers by N-Butanol Additive for Improving $CH_3NH_3PbI_3$ Light Harvesters of Perovskite Solar Cells. *RSC Adv.* **2016**, *6*, 89609−89613.

(19) Zhang, T.; Yang, M.; Zhao, Y.; Zhu, K. Controllable Sequential Deposition of Planar $CH_3NH_3PbI_3$ Perovskite Films Via Adjustable Volume Expansion. *Nano Lett.* **2015**, *15*, 3959−3963.

(20) Zhang, H.; Mao, J.; He, H.; Zhang, D.; Zhu, H. L.; Xie, F.; Wong, K. S.; Gratzel, M.; Choy, W. C. H. A Smooth $CH_3NH_3PbI_3$ Film Via a New Approach for Forming the PbI_2 Nanostructure Together with Strategically High CH_3NH_3I Concentration for High Efficient Planar-Heterojunction Solar Cells. *Adv. Energy Mater.* **2015**, *5*, 1501354.

(21) Wu, Y.; Islam, A.; Yang, X.; Qin, C.; Liu, J.; Zhang, K.; Peng, W.; Han, L. Retarding the Crystallization of PbI_2 for Highly Reproducible Planar-Structured Perovskite Solar Cells Via Sequential Deposition. *Energy Environ. Sci.* **2014**, *7*, 2934−2938.

(22) Fu, Y.; Meng, F.; Rowley, M. B.; Thompson, B. J.; Shearer, M. J.; Ma, D.; Hamers, R. J.; Wright, J. C.; Jin, S. Solution Growth of Single Crystal Methylammonium Lead Halide Perovskite Nanostructures for Optoelectronic and Photovoltaic Applications. *J. Am. Chem. Soc.* **2015**, *137*, 5810−5818.

(23) Dualeh, A.; Tétreault, N.; Moehl, T.; Gao, P.; Nazeeruddin, M. K.; Gratzel, M. Effect of Annealing Temperature on Film Morphology of Organic−Inorganic Hybrid Perovskite Solid-State Solar Cells. *Adv. Funct. Mater.* **2014**, *24*, 3250−3258.

(24) Williams, S. T.; Zuo, F.; Chueh, C.-C.; Liao, C.-Y.; Liang, P.-W.; Jen, A. K. Y. Role of Chloride in the Morphological Evolution of Organo-Lead Halide Perovskite Thin Films. *ACS Nano* **2014**, *8*, 10640−10654.

(25) Xu, Y.; Zhu, L.; Shi, J.; Lv, S.; Xu, X.; Xiao, J.; Dong, J.; Wu, H.; Luo, Y.; Li, D.; Meng, Q. Efficient Hybrid Mesoscopic Solar Cells with Morphology-Controlled $CH_3NH_3PbI_{3-X}Cl_x$ Derived from Two-Step Spin Coating Method. *ACS Appl. Mater. Interfaces* **2015**, *7*, 2242−2248.

(26) Shi, T.; Yin, W.-J.; Yan, Y. Predictions for P-Type $CH_3NH_3PbI_3$ Perovskites. *J. Phys. Chem. C* **2014**, *118*, 25350−25354.

(27) Navas, J.; Sanchez-Coronilla, A.; Gallardo, J. J.; Martin, E. I.; Hernandez, N. C.; Alcantara, R.; Fernandez-Lorenzo, C.; Martin-Calleja, J. Revealing the Role of Pb^{2+} in the Stability of Organic-Inorganic Hybrid Perovskite $CH_3NH_3Pb_{1-X}Cd_xI_3$: An Experimental and Theoretical Study. *Phys. Chem. Chem. Phys.* **2015**, *17*, 23886−23896.

(28) Harms, H. A.; Tetreault, N.; Pellet, N.; Bensimon, M.; Gratzel, M. Mesoscopic Photosystems for Solar Light Harvesting and Conversion: Facile and Reversible Transformation of Metal-Halide Perovskites. *Faraday Discuss.* **2014**, *176*, 251−269.

(29) Dunlap-Shohl, W. A.; Younts, R.; Gautam, B.; Gundogdu, K.; Mitzi, D. B. Effects of Cd Diffusion and Doping in High-Performance Perovskite Solar Cells Using Cds as Electron Transport Layer. *J. Phys. Chem. C* **2016**, *120*, 16437−16445.

(30) Arend, H.; Huber, W.; Mischgofsky, F. H.; Richter-Van Leeuwen, G. K. Layer Perovskites of the $(C_nH_{2n+1}NH_3)_2MX_4$ and $NH_3(CH_2)_mNH_3MX_4$ Families with M = Cd, Cu, Fe, Mn or Pd and X = Cl or Br: Importance, Solubilities and Simple Growth Techniques. *J. Cryst. Growth* **1978**, *43*, 213−223.

(31) Trentler, T. J.; Hickman, K. M.; Goel, S. C.; Viano, A. M.; Gibbons, P. C.; Buhro, W. E. Solution-Liquid-Solid Growth of

Crystalline III-V Semiconductors: An Analogy to Vapor-Liquid-Solid Growth. *Science* **1995**, *270*, 1791−1794.

(32) Saliba, M.; Matsui, T.; Seo, J.-Y.; Domanski, K.; Correa-Baena, J.-P.; Nazeeruddin, M. K.; Zakeeruddin, S. M.; Tress, W.; Abate, A.; Hagfeldt, A.; Gratzel, M. Cesium-Containing Triple Cation Perovskite Solar Cells: Improved Stability, Reproducibility and High Efficiency. *Energy Environ. Sci.* **2016**, *9*, 1989−1997.

(33) Jacobsson, T. J.; Correa-Baena, J.-P.; Halvani Anaraki, E.; Philippe, B.; Stranks, S. D.; Bouduban, M. E. F.; Tress, W.; Schenk, K.; Teuscher, J.; Moser, J.-E.; Rensmo, H.; Hagfeldt, A. Unreacted PbI_2 as a Double-Edged Sword for Enhancing the Performance of Perovskite Solar Cells. *J. Am. Chem. Soc.* **2016**, *138*, 10331−10343.

(34) Chen, Q.; Zhou, H.; Hong, Z.; Luo, S.; Duan, H.-S.; Wang, H.-H.; Liu, Y.; Li, G.; Yang, Y. Planar Heterojunction Perovskite Solar Cells Via Vapor-Assisted Solution Process. *J. Am. Chem. Soc.* **2014**, *136*, 622−625.

(35) Hwang, S. H.; Roh, J.; Lee, J.; Ryu, J.; Yun, J.; Jang, J. Size-Controlled SiO_2 Nanoparticles as Scaffold Layers in Thin-Film Perovskite Solar Cells. *J. Mater. Chem. A* **2014**, *2*, 16429−16433.